Monthly Weather Review

Supporting Information for

The impact of the extreme winter 2015/2016 Arctic cyclone on the Barents-Kara seas

Linette N. Boisvert[1,2] , Alek A. Petty[1,2] and Julienne C. Stroeve[3,4]

[1] Earth System Science Interdisciplinary Center, University of Maryland, College Park MD 20740 U.S.A.

[2] National Aeronautics and Space Administration, Goddard Space Flight Center, Greenbelt, MD, U.S.A.

[3] National Snow and Ice Data Center, Cooperative Institute for Research in Environmental Sciences, Campus Box 499, University of Colorado, Boulder, CO 80309-0449 U.S.A.

[4] Centre for Polar Observation and Modeling, Pearson Building, University College London, Gower St., London WC1E6BT, UK

Contents of this file

Text S1 to S7
Table S1
Figures S1 to S4

Introduction

This supplemental section provides more detail on the various data products used in this study, including: the Atmospheric Infrared Sounder (AIRS) data products and how the blended near surface specific humidity and air temperature data were created (Text S1), the ice concentration and ice drift product description (Text S2), an explanation of why downwelling is used instead of SEB for the elevated events (Text S4), a description of the freeze onset data (Text S5), a short description of the role of the ocean (Text S6) and PIOMAS and SMOS ice thickness data (Text S7). Text S3 explains how all of the surface energy balance terms are computed in detail. Text S7 also describes the toy sea ice model used. The rest of the supplemental section contains Figures S1-S4, which could not be included in the main body of the text due to length restrictions, but are still useful for the reader to reference.

Text S1.

AIRS is a cross-track, high spectral resolution, infrared sounder onboard NASA's Aqua satellite, launched on 04 May 2002. AIRS has 2378 infrared channels and collects radiance data with a 13.5 km spatial resolution in the horizontal at nadir [*Susskind et al.,* 2011]. AIRS global retrievals are made twice daily in ascending and descending orbits and can accurately retrieve data under most cloud conditions without the need for surface classifications, thus reducing errors [*Susskind et al.,* 2014]. This is important in the Arctic, where data is sparse, the surface type (ice and ocean) continually changes, and clouds are prevalent, especially along storm tracks. AIRS data products of skin temperature and specific humidity have been compared to a variety of in-situ observations in the Arctic and have show to produce accurate results [*Boisvert et al.,* 2015].

To obtain accurate retrievals from an IR instrument its footprint has to be cloud free. This can cause problems in the Arctic where clouds are prevalent, especially during cyclones. In order to increase spatial coverage, the AIRS science team has implemented a cloud-clearing technique that uses the nine 15 km hyperspectral IR measurements (AIRS) inside a 50 km multichannel microwave footprint (AMSU) [*Susskind et al*., 2014]. This technique takes advantage of cloud inhomogeneity in a smooth clear-sky background to estimate what cloud-clear radiances should be as cloud fraction approaches zero, even where all nine IR footprints are cloudy. However, errors will become large when there is little to no fluctuation of cloud cover in the nine AIRS footprints and retrievals can't be made. During times when there is high cloud cover, and little heterogeneity, AIRS will produce bad retrievals, and thus lose data coverage. This scenario is seen during the winter storm in the near surface temperature and humidity products.

When data gaps exist in the near-surface daily temperature and humidity estimates, due in part to an abundance of homogeneous clouds in the AIRS footprint, they are supplemented with data products taken from the standard 700 hPa pressure level. Using an iterative method to estimate their subsequent values near the surface [*Launiainen and Vihma*, 1990], the daily 700 hPa temperature and humidity products are used to fill in data gaps present in the near surface products. Using this method, along with the height at which the variables were observed (i.e. 700 hPa geopotential height), and information on the stability of the boundary layer, the temperature and humidity at 2 m is estimated. When there is missing or bad data, specifically around the "pole hole", this data is omitted in the figures and calculations. Some data gaps remain even in the 700 hPa data products when the retrieval is flagged as not good or of the best quality, and are therefore not processed in the data product. This method removes a significant fraction of the original data gaps, but a few still remain.

When the AIRS level 3 daily files are gridded onto a polar projection, there will always be a discontinuity at 180 ^{o}E because of the near 24-hour time difference in the satellite pass. The discontinuities may be more noticeable during the height of the cyclone, which is rapidly changing the atmospheric environment within a day. This is outside of our BaKa study region, however.

Text S2.

Both sea ice concentration (SIC) datasets are produced using the NASA team algorithm and are made available at the National Snow and Ice Data Center (NSIDC). The daily concentration data are converted to extent (as in Figure 1) by defining the area of all grid cells with at least 15% SIC.

CERSAT provide drift estimates from the feature tracking of ice parcels using various combinations of passive microwave brightness data and scatterometry data, across different polarizations [*Girard-Ardhuin and Ezraty, 2012*]. The CERSAT merging technique is utilized to increase reliability and spatial coverage in the final product. We use the NRT CERSAT/AMSR2 drift data (produced using merged horizontal and vertical polarizations of Advanced Microwave Scanning Radiometer (AMSR2) data), due to its high spatial resolution (6.25 km) and lower daily lag (2-days) in the tracking of ice features. The NRT daily drifts were averaged over a one-month period covering the duration of the storm (20th December-20th January, 2016). We use a longer period than the storm duration to increase data coverage in the Barents-Kara Seas region, where gaps in the CERSAT/AMSR-2 drift data are common.

Another near real time drift product is produced using the C-band Advanced Scatterometer (ASCAT). The higher resolution (62.5 km) ASCAT drift estimates were also analyzed (not shown) and produced similar results to those discussed in the main text.

Text S3.

Calculation of terms in the surface energy balance.

$$F_r + F_L + F_E + F_s + F_e = SEB \qquad \text{(S1)}$$

F_r is the net absorbed shortwave flux

$$F_r = SWD(1-\alpha) = 0 \qquad \text{(S2)}$$

where SWD is the shortwave downwelling radiation and α is the albedo. F_r is absent in the BaKa region for this time period due to polar night, and is thus set to zero.

Following *Maykut and Church* [1973], we define the downwelling longwave flux term, F_L

$$F_L = \sigma \varepsilon_d T_a^4 \qquad \text{(S3)}$$

where σ is the Stefan-Boltzmann constant, T_a is the air temperature at the “screen height”, which is defined by *Maykut and Church* [1973] as the temperature between 1.5-2m above the surface. Thus we use near surface air temperature from AIRS data. ε_d is the emissivity of the downward longwave flux and is estimated empirically by *Maykut and Church* [1973] using five years of radiation data taken from Point Barrow, Alaska as

$$\varepsilon_d = 0.7829(1 + 0.2232 C_F^{2.75}) \qquad \text{(S4)}$$

where C_F is the cloud fraction (from AIRS data),

The emitted longwave (blackbody) radiation F_E, is given by

$$F_E = \epsilon \sigma T_0^4 \qquad \text{(S5)}$$

where $\epsilon$is the longwave emissivity of the surface layer, which we take to be 0.99, σ is the Stefan-Boltzmann constant, and T_0 is the surface temperature, taken from AIRS data.

The Monin-Obukhov similarity theory, which characterizes the vertical behavior of nondimensionalized mean flow and the turbulence properties in the surface layer of the atmosphere [*Monin and Obukhov*, 1954], is used to estimate the turbulent fluxes (S5, S6, given below) in the atmospheric boundary layer. The magnitude of equations S5 and S6 thus depend on the difference in specific humidity (or temperature) between the surface and the air as well as the wind speed, surface roughness, and thermal stratification, which determine the intensity of the turbulent transport [*Launiainen and Vihma*, 1994].

The sensible heat flux term, F_S, is given by

$$F_S = \rho c_p U[I_c\, C_{Sz,i}(T_a - T_{0,i}) + (1 - I_C) C_{Sz,w}(T_a - T_{0,w})] \qquad \text{(S6)}$$

where $\rho$is the air density, c_p is the specific heat of air (c_p=1004 J kg^{-1} K^{-1}), $C_{s,i}$ is the sensible heat transfer coefficient over ice and $C_{s,w}$ is the sensible heat transfer coefficient over water (given below), I_C is the ice concentration, U is the 10m wind speed (m s^{-1}) taken from MERRA-2, $T_{0,I}$ is the temperature of the sea ice surface and $T_{0,w}$ is the temperature of the ice-free ocean surface.

The latent heat flux term, F_e, is given by

$$F_e = \rho U[I_c\, C_{Ez,i}\, L_i(q_a - q_{0,i}) + (1 - I_C)C_{Ez,w}L_w(q_a - q_{0,w})] \qquad \text{(S7)}$$

where ρ is the air density, $C_{Ez,i}$ is the latent heat transfer coefficient over ice, $C_{Ez,w\ i}$ is the latent heat transfer coefficient over water (given below), L_i is the latent heat of sublimation (L_i=2.83x10^6 J kg^{-1}) over ice, L_w is the latent heat of vaporization when the surface is water (L_w=2.5x10^6 J kg^{-1}), q_a is the specific humidity of the air near the surface (taken from AIRS data), $q_{0,i}$ is the specific humidity of the sea ice surface and $q_{0,w}$ is the specific humidity of the ice-free ocean surface, where both are calculated using the surface temperature and assuming saturation at the surface.

The sensible and latent heat transfer coefficients are defined by the roughness lengths and stability corrections for stable and unstable conditions for either sea ice or ocean surfaces and are given by *Launiainen and Vihma* [1990] as

$$C_{Sz} = C_S\left(z, z_0, z_T, \Psi_M\left(\frac{z}{L}\right), \Psi_S\left(\frac{z}{L}\right)\right) = k^2 \Big/ \left[\ln\left(\frac{z}{z_0}\right) - \Psi_M\left(\frac{z}{L}\right)\right]\left[\ln\left(\frac{z}{z_T}\right) - \Psi_S\left(\frac{z}{L}\right)\right] \qquad \text{(S8)}$$

$$C_{Ez} = C_E\left(z, z_0, z_q, \Psi_M\left(\frac{z}{L}\right), \Psi_E\left(\frac{z}{L}\right)\right) = k^2 \Big/ \left[\ln\left(\frac{z}{z_0}\right) - \Psi_M\left(\frac{z}{L}\right)\right]\left[\ln\left(\frac{z}{z_q}\right) - \Psi_E\left(\frac{z}{L}\right)\right] \qquad \text{(S9)}$$

where z is the measuring height (2m), z_0, z_T, and z_q are the roughness lengths for the wind speed, temperature and water vapor, L is the Obukhov length and Ψ_M, Ψ_S and Ψ_E are the integrated universal functions of wind, temperature and humidity based on the stability of the boundary layer. In the stable case, the universal functions are defined by *Holtslag and de Bruin* [1988] and for the unstable case are defined by *Paulson* [1970], *Businger et al.* [1971] and *Dyer* [1974]. Thus these transfer coefficients are defined by the roughness lengths and the stability corrections in stable and unstable conditions [*Launiainen and Vihma,* 1994].

z_0 is based on the interaction between the wind and wave field. If the surface is ice-free, then z_0 depends on C_D [*Large and Pond,* 1980].

$$\ln(z_0) = \ln(z) - kC_D^{-1/2} \qquad \text{(S10)}$$

where C_D is dependent on the wind speed at 10 meters: $C_D x 10^{-3} = 0.61 + 0.063U$ and C_E and C_S depend on C_D: $C_E = C_S = 0.63C_D + 0.32x10^{-3}$ and z_T and z_q depend on both $C_{E,S}$ and C_D.

$$\ln(z_T) = \ln(z_q) = \ln(z) - kC_D^{-1/2}C_{E,S}^{-1} \qquad \text{(S11)}$$

If the surface is snow/ice then z_0 is calculated by (S12) where C_D depends on the snow/ice surface roughness (ξ),

$$C_D x 10^{-3} = 1.10 + 0.072\xi \qquad \text{(S12)}$$

The Reynolds number (R_e) [*Andreas,* 1987] is used to calculate z_T and z_q. R_e gives an estimate for how far the roughness elements come above the molecular sublayer. When R_E is small, viscous forces dominate and the flow is smooth and constant, when it is large inertial forces dominate and the flow is turbulent and chaotic. The coefficient values in S13 are shown in Table S1.

$$\ln(z_T) = \ln(z_q) = \ln(z_0) + b_0(R_e) + b_1(R_e)\ln(R_e) + b_2(R_e)(\ln(R_e))^2 \qquad \text{(S13)}$$

It is important to note S5 and S6 use the "mosaic" method to account for both sea ice and ice-free ocean in each ocean grid box [*Vihma*, 1995], using the sea ice concentrations from SSMI. *Vihma* [1995] compared results from the mosaic method with results from an atmospheric model and found that the mosaic method performed well in comparison with a 2-d hydostatic mesoscale planetary boundary layer model and *Zulauf and Krueger* [2003] found that the mosaic method similar to the one used here produced physically equivalent results compared to an idealized case produced using a 2-d cloud-resolving model and Surface Heat Budget of the Arctic Ocean (SHEBA) data over large areas of the marginal sea ice zones.

Text S4.

When analyzing the SEB for the 2015/2016 cyclone compared to other elevated events between 2003-2016, the storm does not seem as extreme, however. This is due to the anomalously high December skin temperatures in the region, which were ~2.5 ^{o}C greater than the average (2003-2014). These warmer skin temperatures (compared to earlier years) significantly reduce the magnitude of the sensible and latent heat fluxes, and increase the upwelling longwave heat flux, acting as negative feedback.

Text S5.

Freeze onset data from 2003-2015 are updated from *Stroeve et al.* [2014] and the full algorithm description is discussed in *Markus et al.* [2009]. This data is produced using microwave brightness temperatures from the Special Sensor Microwave Imager and Sounder (SSMIS). The data give the day of the year for each 25 km^2 pixel when freeze-up of the sea ice/ice-free ocean begins. The freeze onset of new ice is flagged as the day of the year when the ice concentration in that pixel reaches greater than or equal to 80% [*Markus et al*., 2009]. Along the ice edge of the BaKa region the sea ice concentration can be less than 80%, and is therefore not included in the freeze onset map (Figure S4).

Text S6.

Årthun et al. [2012] demonstrated that the Barents Sea ice variability is strongly controlled by the influx of ocean heat into the region. Skillful predictions of the Barents Sea ice cover were recently demonstrated using observations of the inflow of warm Atlantic water through the Barents Sea Opening [*Onarheim et al.,* 2015]. A lower 2016 winter ice cover (compared to 2015) was predicted in that study.

Text S7.

Our estimated sea ice thickness response (an approximate budget scaling) is simplified by neglecting sea ice heat capacity and assuming negligible heat conduction through the ice (a reasonable assumption considering the near freezing skin temperatures shown in Figure S4). The estimated thickness changes can be expressed by

$$\delta h = -\delta Q_i/(\rho L_f) \tag{S14}$$

where δQ_i is the mean SEB over sea ice covered BaKa region (shown earlier in Figures 4 and 6), ρ is the density of ice (930 kg m^{-3}) and L_f is the latent heat of fusion of sea ice (3.2x10^{-5} J m^{-3}).

We use sea ice thickness estimates from the Pan-Arctic Ice-Ocean Modeling and Assimilation System (PIOMAS, v2.1) [*Schweiger et al.,* 2011]. PIOMAS is an ice-ocean model, producing ice thickness estimates constrained predominantly by the assimilation of sea ice concentration and sea surface temperature. We use the daily data from 28th December 2015 to 6th January 2016.

We also use the thin sea ice thickness estimates using brightness temperature measurements from the Microwave Imaging Radiometer using Aperture Synthesis (MIRAS) onboard ESA's Soil Moisture and Ocean Salinity (SMOS) satellite [*Tian-Kunze et al.,* 2016]. Data with an uncertainty greater than 1 m, or with a ratio between retrieved and maximum retrievable sea ice thickness near 100% are masked, following the data uncertainty description given in the data portal (http://icdc.zmaw.de/1/daten/cryosphere/l3c-smos-sit.html). Note that the thin-ice thickness estimates in the Barents Sea region have recently been validated by *Kaleschke et al.* [2016].

To further investigate these regional thickness declines, we also analyzed the daily thin-ice thickness estimates from ESA's Soil Moisture and Ocean Salinity (SMOS) satellite [*Tian-Kunze et al.,* 2016], as shown in Figure 6. This shows similar regional thickness declines to the PIOMAS estimates (up to 50 cm in the Barents Sea), further suggesting a thinning of the sea ice in the BaKa region, driven by this anomalous SEB.

References

Andreas, E. L. (1987), A theory for the scalar roughness and the scalar transfer coefficients over the snow and ice, *Bound.-Layer Meteor.*, 38, 159-184.

Årthun, M., T. Eldevik, L. H. Smedsrud, Ø. Skagseth, and R. B. Ingvaldsen (2012), Quantifying the influence of Atlantic heat on Barents sea ice variability and retreat, *J. of Clim.*, *25*(13), 4736-4743.

Boisvert, L. N., D. L. Wu, T. Vihma, and J. Susskind (2015), Verification of air/surface humidity differences from AIRS and ERA-Interim in support of turbulent flux estimation in the Arctic, *J. Geophys. Res. Atmos.*, 120, doi:10.1002/2014JD021666.

Businger, J. A., J. C. Wyngaard, Y. Izumi, and E. F. Bradley (1971), Flux-profile relationships, *J. Atmos. Sci.*, 28, 181-189.

Dyer, A. J. (1974), A review of flux-profile relationships, *Bound.-Layer Meteor.*, 7, 363-372.

Girard-Ardhuin, F., and R. Ezraty (2012), Enhanced Arctic sea ice drift estimation merging radiometer and scatterometer data, *IEEE Transactions on Geoscience and Remote Sensing*, 50:7, pp 2639-2648, doi:10.1109/TGRS.2012.2184124.

Holtslag, A. A. M., and H. A. R. de Bruin (1988), Applied modeling of the nighttime surface energy balance over land, *J. Appl. Meteorol.*, 37, 689– 704.

Kaleschke, L., Tian-Kunze, X., Maaß, N., Beitsch, A., Wernecke, A., Miernecki, M., ... & Pohlmann, T. (2016). SMOS sea ice product: Operational application and validation in the Barents Sea marginal ice zone. *Remote Sensing of Environment*.

Large, W. G. and S. Pond (1980), Open ocean momentum flux measurements in moderate to strong winds, *J. Phys. Oceanogr.*, 11, 324-336.

Launiainen, J., and T. Vihma (1990), Derivation of turbulent surface fluxes—An iterative flux-profile method allowing arbitrary observing heights, *Environ. Software*, 5, 113–124.

Launiainen, J., and T. Vihma (1994), On the surface heat fluxes in the Weddell Sea, *The Polar Oceans and Their Role in Shaping the Global Environment*, Nansen Centennial Volume, Geophysical Monogram Series, 85, edited by O.M. Johannessen, R. Muench, and J.E. Overland, pp., 399-419, AGU, Washington, D.C.

Markus, T., J. C. Stroeve, and J. Miller (2009), Recent changes in Arctic sea ice melt onset, freeze-up, and melt season length, *J. Geophys. Res.*, 114, C07005, doi:10.1029/2009JC005436.

Maykut, G. A., and P. E. Church (1973), Radiation climate of Barrow, Alaska, 1962–66, *J. Appl. Meteorol.*,12, 620–628.

Monin, A. S. and A. M. Obukhov (1954), Dimensionless characteristics of turbulence in the surface layer, *Trudy Geofiz. Inst. Akad. Nauk.,* 24, 163-187.

Onarheim, I. H., T. Eldevik, M. Årthun, R. B. Ingvaldsen, and L. H. Smedsrud (2015), Skillful prediction of Barents Sea ice cover, Geophys. Res. Lett., 42, 5364–5371, doi:10.1002/2015GL064359.

Paulson, C. A. (1970), The mathematical representation of wind speed and temperature profiles in the unstable atmospheric surface layer, *J. Appl. Meteor.,* 9, 857-861.

Schweiger, A., R. Lindsay, J. Zhang, M. Steele, H. Stern, and R. Kwok (2011), Uncertainty in modeled Arctic sea ice volume, *J. Geophys. Res*., 116, C00D06, doi:10.1029/2011JC007084.

Stroeve, J. C., T. Markus, L. Boisvert, J. Miller, and A. Barrett (2014), Changes in Arctic melt season and implications for sea ice loss, *Geophys. Res. Lett*., 41, 1216–1225, doi:10.1002/2013GL058951.

Susskind, J., J. M. Blaisdell, and L. Iredell (2014), Improved methodology for surface and atmospheric soundings, error estimates, and quality control procedures: the atmospheric infrared sounder science team version-6 retrieval algorithm, *J. Appl. Remote Sens.*, 8(1), 084994, doi:10.1117/1.JRS.8.084994.

Susskind, J., J. M. Blaisdell, L. Iredell, and F. Keita (2011), Improved Temperature Sounding and Quality Control Methodology using AIRS/AMSU data: The AIRS Science Team Version 5 Retrieval Algorithm, *IEEE Transactions on Geoscience and Remote Sensing*, 49, 3, pp. 883-907, doi:10.1109/TGRS.2010.2070508.

Tian-Kunze, X., L. Kaleschke, and N. Maass (2013), updated 2016. SMOS Daily sea ice thickness. ICDC, http://icdc.zmaw.de, University of Hamburg, Germany, Digital media.

Vihma, T. (1995), Subgrid parameterization of surface heat and momentum fluxes over polar oceans, *J. Geophys. Res.*, **100**(C11), 22, 625–22,646, doi:10.1029/95JC02498.

Zulauf, M. A., and S. K. Krueger (2003), Two-dimensional cloud-resolving modeling of the atmospheric effects of Arctic leads based upon midwinter conditions at the Surface Heat Budget of the Arctic Ocean ice camp, *J. Geophys. Res.*, **108**(D10), 4312, doi:10.1029/2002JD002643.

Table S1. Values of the coefficients in S12 for estimating the scalar roughness lengths in the three aerodynamic regimes. Values taken from *Andreas* [1987].

R_e	b_0	b_1	b_2
R_e < 0.135 (Smooth)	1.43	0	0
0.135 < R_e < 2.5 (Transition)	0.25	-0.589	0
2.5 < R_e < 1000 (Rough)	0.356	-0.538	-0.181

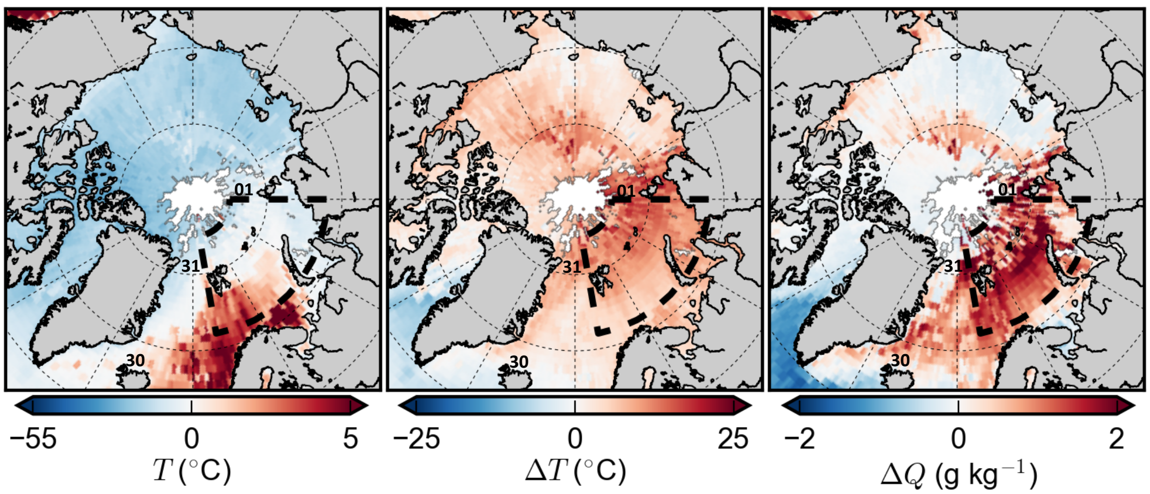

Figure S1. Mean near-surface air temperature (left), air temperature anomalies (middle), and near surface specific humidity anomalies (right) for 30 December 2015 – 01 January 2016. Anomalies (middle and right) are respect to the 2003-2014 mean. The center of the cyclone is located by "30" for 30 December 2015, "31" for 31 December 2015 and "01" for 01 January 2016.The BaKa region is given by the dashed boxes. White areas are no data.

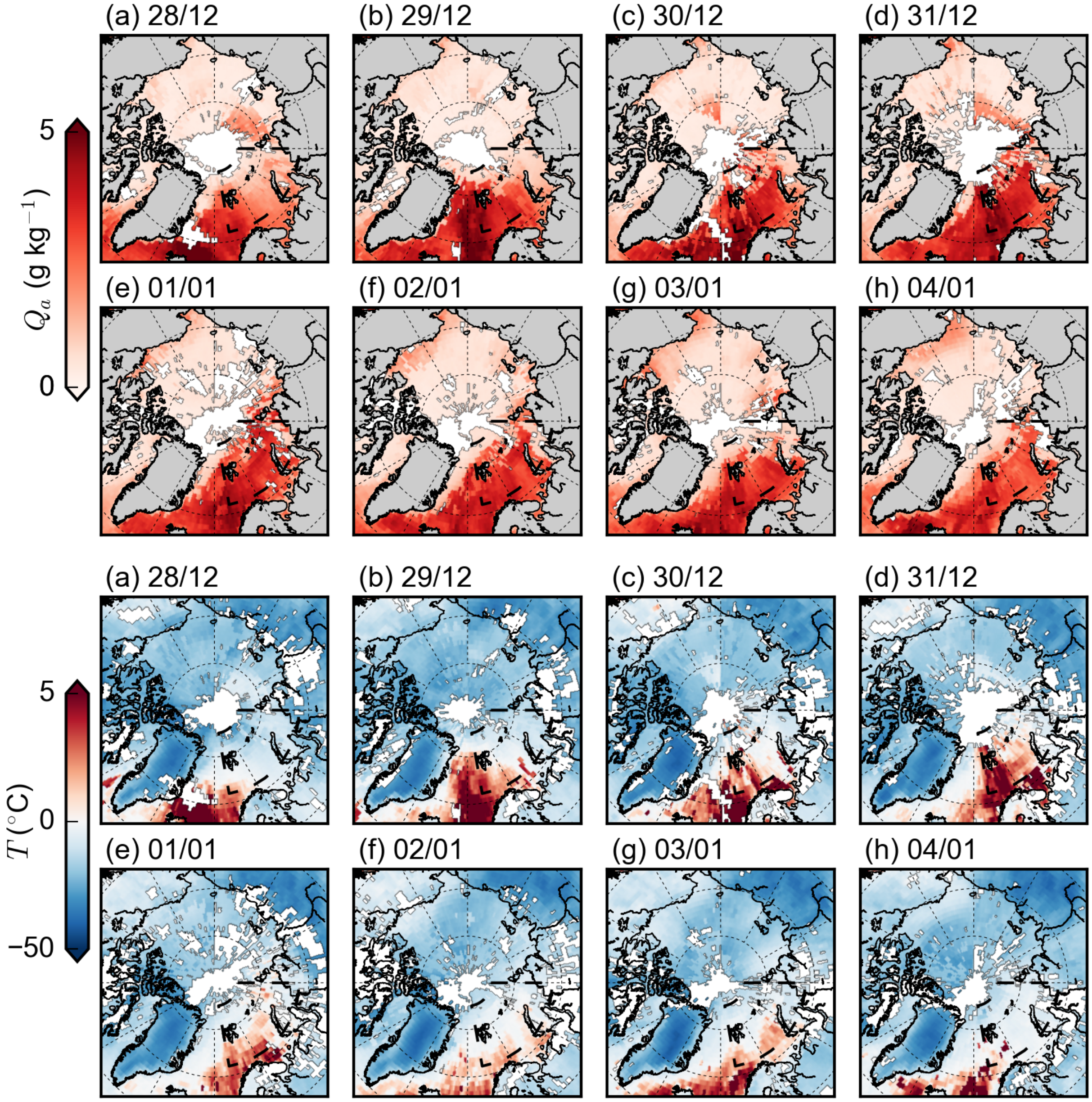

Figure S2. Daily near-surface specific humidity (top) and daily near-surface air temperature (bottom) for 27 December 2015 through 04 January 2016. White areas are no data. Note the non-linear color scale used in the temperature maps.

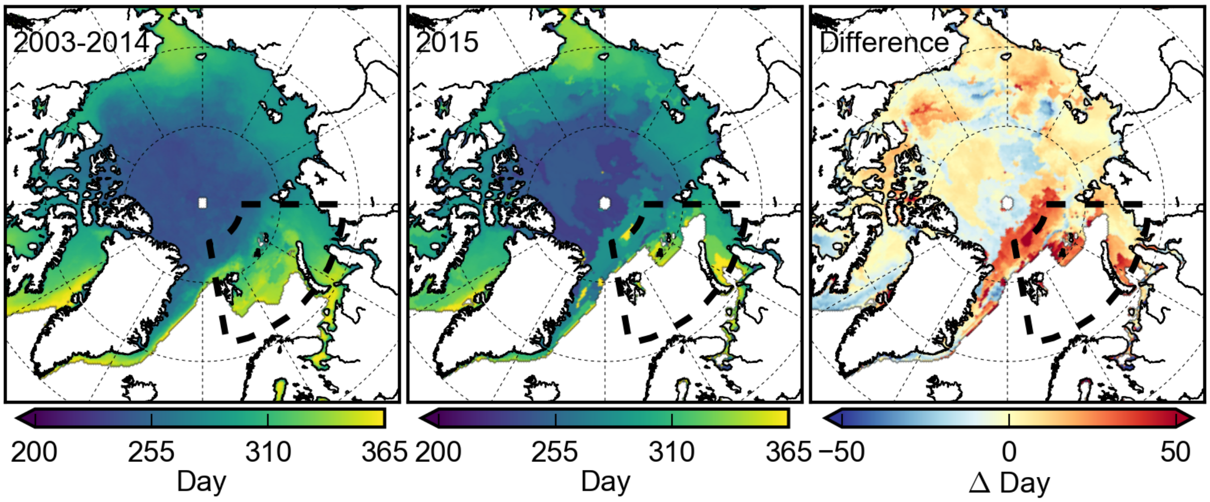

Figure S3. Mean freeze onset averaged over 2003-2014 (left), 2015 Freeze onset (middle) and their difference (2015 minus 2004-2014) (right).

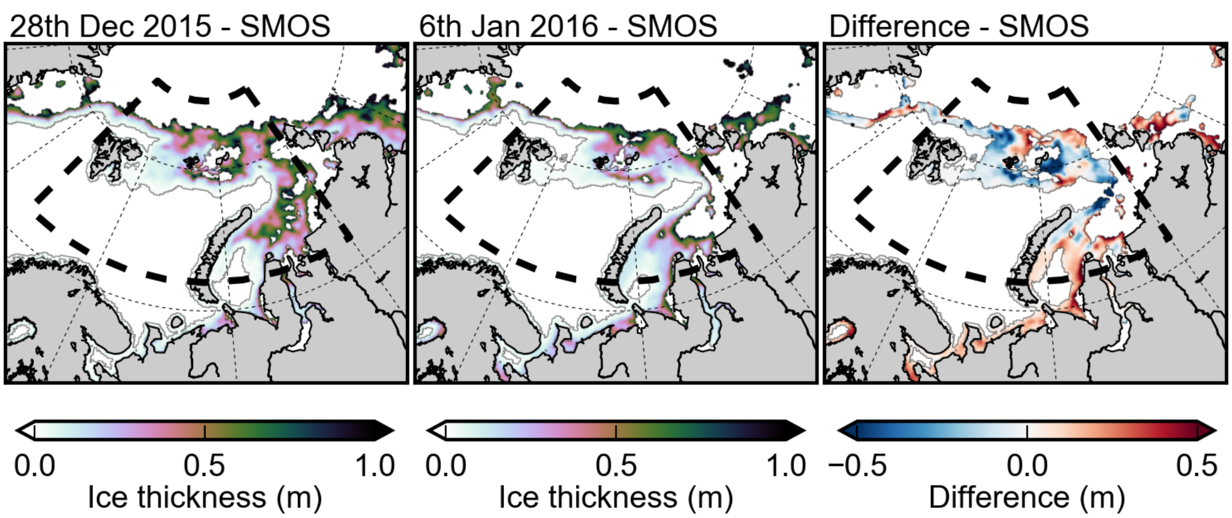

Figure S4. SMOS thin ice thickness maps for the Baka region on 28 December 2015 and 06 January 2016 and the ice thickness difference between the two days.